

# Efficiently Serving Large Multimodal Models Using EPD Disaggregation

Gursimran Singh\* Xinglu Wang† Yifan Hu\* Timothy Yu\* Linzi Xing\* Wei Jiang‡  
Zhefeng Wang‡ Xiaolong Bai‡ Yi Li‡ Ying Xiong\* Yong Zhang\* Zhenan Fan\*

\*Huawei Technologies Canada, †Simon Fraser University, ‡Huawei Cloud

{gursimran.sing1, xinglu.wang, ivan.hu2, timothy.yu, linzi.xing, jiangwei160,  
wangzhefeng, baixiaolong1, alick.li, yingx1211, yong.zhang3, zhenan.fan1}@huawei.com

## Abstract

Large Multimodal Models (LMMs) extend Large Language Models (LLMs) by handling diverse inputs such as images, audio, and video, but at the cost of adding a multimodal encoding stage that increases both computational and memory overhead. This step negatively impacting key Service Level Objectives (SLOs) like time to first token (TTFT) and end-to-end throughput (E2ETP). We introduce Encode-Prefill-Decode (EPD) Disaggregation, a novel framework that separates the encoding, prefill, and decode stages onto dedicated resources. Unlike current systems, which bundle encoding and prefill together, our approach decouple these steps unlocking new opportunities and optimizations. These include a new mechanism to cache multimedia tokens for efficient transfer, a novel way to parallelize encoding load within a request, a module to find the optimal resource allocation for disaggregated serving, and a novel role switching method to handle changing workload characteristics. Experimental evaluations with popular LMMs show substantial gains in memory efficiency (up to  $15\times$  less utilization), batch sizes (up to  $22\times$  larger),  $10\times$  more images/request, and  $2.2\times$  larger KV caches. Further, it leads to significant improvements in latency metrics (TTFT up to 71% reduction) and end-to-end throughput (up to 57% reduction), compared to systems that do not disaggregate.

## 1. Introduction

Large Language Models (LLMs) have revolutionized language understanding and reasoning, achieving superhuman performance across a variety of tasks [1, 4]. Recently, the scope of these models has expanded to include multiple modalities, such as images, audio, and videos, resulting in the advent of Large Multimodal Models (LMMs) [5, 11, 19]. LMMs enable users to interact with diverse data types, such as posing questions about visual scenes or

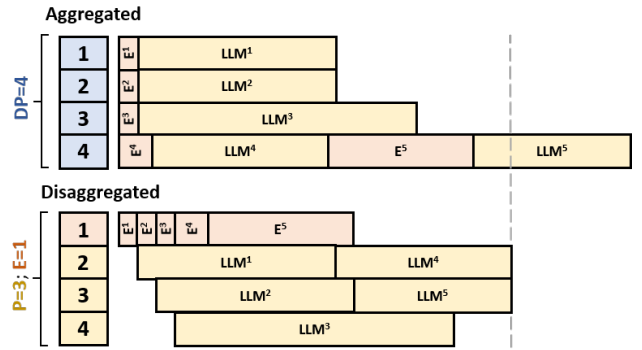


Figure 1. Above: Aggregated system, where E and LLM are coupled and must run on the same GPU. Below: Disaggregated system, where E runs on the 1st GPU and LLM runs on the rest of three GPUs. Multimodal encoder and LLM are denoted by E and LLM, respectively.

analyzing audio clips, thereby unlocking novel applications across fields like healthcare, autonomous systems, and creative industries.

However, serving LMMs in an efficient manner presents unique challenges. Meeting strict Service Level Objectives (SLOs) such as end-to-end throughput (E2ETP), time to first token (TTFT), and time per output token (TPOT) becomes increasingly difficult given the additional computational and memory demands introduced by processing multimodal data [12]. Unlike LLMs, where inference involves prefill and decoding stages, LMMs require an additional encoding stage to process raw multimodal inputs (e.g., images or videos) into tokenized representations. This stage is computationally intensive, especially for high-resolution or complex multimodal inputs, and often produces a substantial number of additional tokens [17]. The resulting increase in tokens inflates resource consumption and leads to quadratic growth in prefill-stage compute demands, adversely impacting SLO attainment.

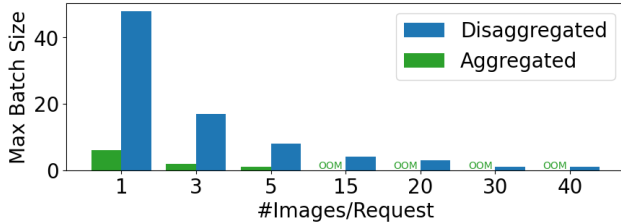


Figure 2. Impact of disaggregation on batch size and number of images/request for the MiniCPM-V 2.6 model

Disaggregating the prefill stage from the decode stage has emerged as a well-studied solution in the literature to improve inference efficiency for LLMs [6, 7, 14, 15, 21]. By assigning separate resources to each stage, prefill-decode disaggregation enables independent optimization of batching, scheduling, and resource allocation strategies, significantly enhancing system throughput and memory utilization. However, these techniques fail to address the challenges of LMM deployment, where the addition of an encoding stage fundamentally alters the resource dynamics. The encoding stage, with its high computational and memory overhead, introduces token inflation and dependency bottlenecks that ripple across subsequent stages, necessitating a rethinking of disaggregation strategies to accommodate multimodal workloads.

These challenges of LLM deployment present opportunities for optimization that current serving systems do not consider. Currently, the encode and prefill stages are aggregated into a single monolithic and synchronous step executed on the same set of GPUs. Sequential execution of encoding and prefilling introduces interference. This interference is demonstrated graphically in Figure 1. In the aggregated approach (Figure 1 top), the prefill step ( $LLM^4$ ) interferes with the encode-heavy request ( $E^5$ ). As a result, such aggregation leads to suboptimal resource utilization and poor SLO performance, revealing that current solutions are inadequate for LMM workloads. By disaggregating encode from prefill, the system may be optimized to reduce interferences for specific workloads. From another perspective, simultaneous loading of both the Multimodal encoder (MME) and LLM onto the same GPUs in aggregated setups restricts memory for processing multiple high resolution images or larger batch sizes. In preliminary investigations, by removing the LLM and associated KV cache, we observe a significant increase in maximum batch sizes and supported number of images/request (Figure 2).

Thus, we propose Encode-Prefill-Decode (EPD) Disaggregation, a framework that decouples the encode, prefill, and decode stages, assigning each with dedicated resources to operate independently. This disaggregation enables customized batching, parallelization, and scheduling strategies for each stage, optimizing resource utilization

while reducing contention. As a result, EPD disaggregation achieves better memory utilization, higher throughput, and improved compliance with critical SLOs like TTFT, TPOT, and E2ETP.

The major contributions of this work are as follows:

- We propose an efficient system for LMM inference that relies on the novel idea of disaggregating encoding and prefill stages. Our approach addresses key challenges of inter-stage communication, efficient parallelization, resource allocation, and performance optimization within this framework.
- We propose intra-request parallelization (IPR) that shards a request into independent encoding jobs which can be executed in parallel, significantly reducing first token latency.
- We formulate the resource allocation problem as an optimization over batch sizes, scheduling strategies, and parallelization approaches for each pipeline stage. Further, we provide a simple black box optimizer that uses workload samples to approximate the optimal config for a given workload.
- We develop dynamic role switching capability that monitors the system for any bottlenecks and allows efficient reallocation of resources between E, P and D stages by efficiently switching ( $\sim 0.7s$ ) the role of an instance among these stages. This ensures system can respond to any changes in workload requirements during online serving.
- We conduct evaluations on various popular LMM models, namely MiniCPM-V 2.6, InternVL2-8B, and InternVL2-26B using real-world and synthetic workloads. The results demonstrate the superiority of our method across various aspects. For instance, our approach requires up to 15x less memory, facilitating up to 22x larger batch sizes, 10x more images/request, and 2.2x larger KV caches. Further, our method significantly improves performance in terms of SLO attainment (up to 90–100% more) and TTFT latency (up to 71% reduction).

## 2. Related Work

In this section, we describe feasible approaches in the literature for multi-modality model serving and their limitations and then review the use of the disaggregation technique.

**Multi-modality Model Serving.** There are two ways to enable a multi-modality model serving system: (1) adopting and extending existing LLM serving systems, such as vLLM [9], SARATHI [2], and Orca [20]; and (2) leveraging the open-sourced code from recent works of improving multi-modality model inference. The first way fails to address the encoding bottleneck inherent in LMMs, limiting their applicability to multimodal workloads, particularly when handling high-volume and high-resolution multi-media data. In the second way, recent advancements such as KV cache eviction [10, 13] and compression [8] fo-

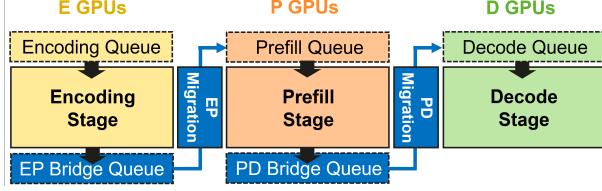


Figure 3. The inference pipeline of EPD Disaggregation.

cus on specific features and limited scenarios. For instance, Inf-MLLM [13] enables efficient streaming inference for LMMs on a single GPU, targeting resource-constrained scenarios. While their implementations are feasible for serving LMMs, they fail to meet user SLOs in cloud serving scenarios. To the best of our knowledge, we are the first to propose an LMM serving system that leverages disaggregation and a series of integrated techniques to enable better resource allocation and improved SLOs.

**Disaggregated Serving.** Disaggregated serving has emerged as a promising technique in large model serving. By decoupling the prefill and decode stages, systems like SplitWise [14], DistServe [21], and DéjàVu [16] mitigate interference between these phases, enabling finer control over Time to First Token (TTFT) and Time Per Output Token (TPOT). However, these systems primarily target LLMs and overlook the encoding step required for LMMs, which is tightly coupled with prefill. Recent work, such as Mooncake [15] and PD-Serve [7], has extended disaggregation to include KV cache management and other system-level optimizations. Despite these advancements, they remain limited in their applicability to LMMs. Disaggregating the encoding phase from prefill could unlock new opportunities for optimizing LMM serving. For instance, when handling requests with long videos, encoding the frames could be executed in parallel, reducing head-of-line blocking and improving overall system efficiency. This approach would enable more flexible batching and scheduling strategies, ultimately achieving better latency and throughput for multimodal workloads.

### 3. Method

In this section, first, we describe the EPD disaggregation framework (Sec. 3.1), followed by a detailed explanation of the system design and optimizations (Sec. 3.2), that includes the asynchronous token transfer, intra-request parallel, optimized resource allocation, and dynamic role switching.

#### 3.1. EPD Disaggregation

As shown in Figure 3, disaggregating an LMM system involves breaking the inference process into multiple stages: *encoding*, *prefill*, and *decode*. Transitions between these stages—*EP-migration* and *PD-migration*—handle the

transfer of data from encoding to prefill and from prefill to decode, respectively. Formally, we denote the input text prompt as  $i_p$ , multimodal data as  $i_m$ , and the text output as  $o$ , and provide details for each step and transition as follows:

**Encoding (E):** The multimodal input  $i_m$  is processed by the MME  $E$ , converting it into multimodal tokens  $v_t^e$  on encoding stage GPUs. These tokens form a high-dimensional multimodal embedding for the next pipeline stage. This process can be denoted as  $v_t^e = E(i_m)$ .

**EP-migration:** Once the  $E$  stage completes processing, the generated multimodal tokens  $v_t^e$  are transferred to the prefill stage  $P$ . This transfer is managed by the *EP-migration* function  $\psi_{EP}$ , which handles the migration of tokens from the encoding worker’s cache to the prefill worker’s cache. This process is expressed as  $v_t^p = \psi_{EP}(v_t^e)$ . Here,  $v_t^p$  represents the tokens in the prefill stage after migration.

**Prefill (P):** The multimodal tokens  $v_t^p$  arrive at the Prefill stage  $P$ , along with the text prompt  $i_p$ . In this stage, the system initializes the Key-Value (KV) cache  $kv_1^p$  and generates the first output token  $o_1^p$ . The KV cache stores context and intermediate states, which are necessary for the subsequent decoding stage. The process is denoted by  $kv_1^p, o_1^p = P(v_t, i_p)$ .

**PD-migration:** After the prefill stage generates the initial token  $o_1^p$  and updates the KV cache to  $kv_1^p$ , the data must be transferred to the decode stage  $D$ . This transfer is managed by the *PD-migration* function  $\psi_{PD}$ , which ensures that the KV cache and the generated token are correctly handed off to the decode worker. This is denoted as  $kv_1^d, o_1^d = \psi_{PD}(kv_1^p, o_1^p)$ .

**Decode (D):** The decode phase  $D$  operates iteratively, using the KV cache  $kv_t^d$  and the token generated in the previous iteration  $o_t^d$  to generate the next token  $o_{t+1}^d$  and update the KV cache to  $kv_{t+1}^d$ . This autoregressive process continues until the desired output sequence is generated, as denoted by  $kv_{t+1}^d, o_{t+1}^d = D(kv_t^d, o_t^d)$ .

#### 3.2. System Design and Optimization

Figure 4 illustrates the architecture of the EPD Disaggregated inference system. Each pipeline stage (Encoding, Prefill, and Decoding) has independent instances that run the corresponding stage. These instances operate in data parallel (DP) mode, enabling concurrent processing of multiple requests per stage and ensuring scalability and efficiency.

Each instance comprises a scheduler, responsible for scheduling requests, block managers (responsible for managing cache(s)), and multiple workers. The workers operate in tensor-parallel (TP) and/or pipeline-parallel (PP) mode, where each worker holds only a subset of the model weights and the corresponding caches required for the stage.

In the encoding stage, workers load only the encoder weights and initialize the Multimodal (MM) cache. In the

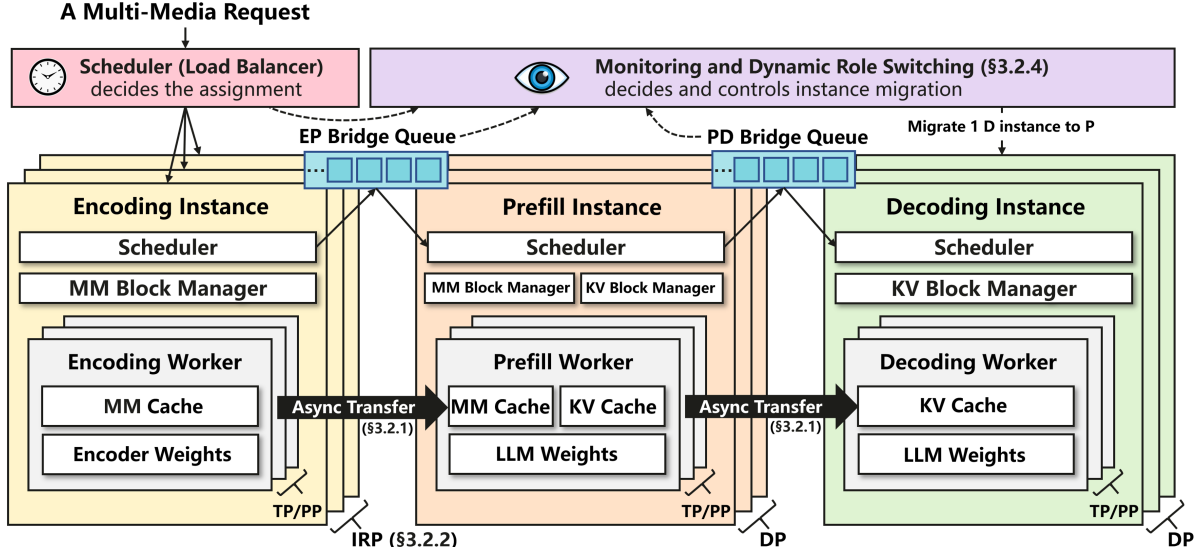


Figure 4. System architecture of the proposed EPD Disaggregated Inference.

prefill stage, the LLM weights are loaded, and both the MM and KV caches are required to efficiently manage all the data associated with the request. In the decoding stage, workers load the LLM weights for decoding tasks and use the KV cache.

Cache transfers occur asynchronously when an instance pulls a request from its queue, ensuring the transfer occurs once the downstream instance is ready. Further, our system incorporates several techniques to optimize the performance of the disaggregated LMM pipeline, with a primary focus on ensuring smooth token transfers between stages (Section 3.2.1), reducing latency (Section 3.2.2), managing resources effectively (Section 3.2.3), and adapting to changing workloads (Section 3.2.4). The ablation of these features are shown in Sec. 4.4.

### 3.2.1. Asynchronous Token Transfer

Disaggregating the system introduces an additional step of transferring vision tokens from the encoding to the prefill stage. To minimize latency during token transfers between stages, our system employs direct, asynchronous transfers via high-bandwidth channels (NVLink, and InfiniBand). The asynchronous transfer allows the system to continue processing new requests without interruption. Both encoding and prefill workers maintain an MM cache to facilitate this process.

When encoding is complete, tokens are stored in the encoding worker’s MM cache, allowing it to serve new requests immediately. An asynchronous event loop monitors completed encoding tasks and initiates direct token transfers to the prefill worker’s MM cache. Once the transfer is confirmed, the encoding cache entries are cleared to free memory. To manage these cache blocks effectively, we introduce the MMBlockManager, which pre-allocates cache

blocks based on each request’s needs. After token transfer, the blocks are reassigned or de-allocated, ensuring flexible cache utilization even under heavy workloads.

### 3.2.2. Intra-Request Parallel (IRP)

Multimodal requests often include multiple high-resolution images in many practical scenarios like autonomous driving and video question answering. In modern LMMs, these images are further converted into a large number of patches that needs to be processed through a computationally-heavy MME. This significantly increases the computation load, making the encoding process a major bottleneck.

To address this, we introduce Intra-Request Parallelism (IRP), which partitions a single request’s image patches across multiple encoding workers in a data-parallel fashion. Since patches are encoded independently, they can be processed and transferred concurrently. Specifically, each encoding worker concurrently processes a subset of patches, computes their token representations, and asynchronously transfers them to the prefill stage. Once all patch-level tokens reach the prefill stage, they are aligned, projected, and merged to form the complete multimodal tokens.

### 3.2.3. Optimized Resource Allocation

The EPD system requires tuning various configurations, including batch sizes, scheduling strategies, and parallelization methods for each pipeline stage. To determine the optimal setup, we collect historical workload samples and apply a black-box optimizer.

Let  $f(\cdot)$  represent the system’s performance metric (e.g., goodput, see Section 4). Since  $f(\cdot)$  is treated as a black-box function with an unknown internal mechanism, we rely on a simulator—extended from DistServe [21]—to evaluate performance metrics efficiently. The objective is to maxi-

mize performance while minimizing GPU usage, which inherently reduces pipeline inefficiencies (e.g., idle time) and improves resource utilization. Formally, we solve

$$\max_{(\mathbf{p}, \mathbf{b}, \mathbf{s}) \in \mathcal{X}} f(\mathbf{p}, \mathbf{b}, \mathbf{s}) - \beta \text{cost}(\mathbf{p}) \quad (1)$$

Here,  $\mathcal{X}$  is the search space for system configs, including parallelization configs  $\mathbf{p}$ , max batch size configs  $\mathbf{b}$ , and scheduling configs  $\mathbf{s}$  (See Appendix A for details). We use Bayesian optimization [3] to solve Problem 1.

### 3.2.4. Dynamic Role Switching

The configuration optimizer described in the previous section can determine the optimal settings for a given workload. However, in an online environment, workload characteristics can change dynamically, requiring adjustments to the configuration. Re-initializing the entire system from scratch in response to these changes can be both difficult and costly. For instance, there may be ongoing requests in the encoding, context, or decoding phases with pre-computed KV and/or VE caches stored in memory. A naive re-initialization would not only involve booting time but also force these requests to restart from the beginning, potentially causing a cascading impact on SLO metrics for subsequent requests.

To overcome these challenges, we introduce dynamic role switching, which enables any instance in the E, P, or D stages to switch roles to any other stage (E, P, or D) with minimal overhead. At a high level, dynamic role switching continuously monitors the system’s queuing statistics across all stages and reallocates workers to stages experiencing higher demand. When a decision is made to transfer an instance from a source stage  $S$  to a destination stage  $T$ , the migration process occurs in three key steps:

- **Offload:** The instance in the  $S$  stage stops accepting new requests and redistributes its queued tasks to sibling instances in the same stage.
- **Migration:** The instance is reconfigured to meet the requirements of the  $T$  stage. This may involve switching both the model and cache type. For example, if the E stage is involved, the instance may switch from an LLM to an MME model and from a KV cache to an MM cache.
- **Onload:** The migrated instance resumes processing new requests, helping to alleviate the queuing bottleneck at the  $T$  stage.

This process typically takes less than 0.7 seconds. The duration is longer for migrations involving the E stage due to model and cache changes, but significantly shorter when switching between P and D stages, as both the LLM and KV cache can be reused.

## 4. Experiments

In this section, we analyze and compare the performance of the proposed EPD disaggregation method against various

baselines. We start with an end-to-end generation performance analysis in Sec. 4.1, followed by an examination of first token latency in Sec. 4.2. We then evaluate the memory savings achieved by EPD in Sec. 4.3. Finally, an ablation analysis of key system components is presented in Sec. 4.4. Additional experiments are detailed in the Appendix, including 1) a throughput comparison in offline settings (Appendix C); 2) an extension of our framework to Neural Processing Units (NPUs) demonstrating a 10% performance improvement (??), and 3) additional SLO and memory experiments (Appendix D).

**Baselines:** We compared the proposed EPD method against two popular baselines: DistServe [21] and vLLM [9]. The DistServe baseline implements the prefill-decode (PD) disaggregation approach, where the prefill and encoding are executed on one set of GPUs, while the decode phase is disaggregated on separate GPUs. Since DistServe was originally designed for LLMs, we extended it to support LMMs by enabling multimodal data processing and modifying the block manager to accommodate multimodal tokens. The vLLM baseline adopts a monolithic architecture, where all three stages run on the same set of GPUs.

**Models:** We utilized three LMMs in our analysis: MiniCPM-V 2.6 [19], InternVL2-8B, and InternVL2-26B [5]. These LMMs are renowned for their advanced capabilities in processing and understanding multimodal data. Detailed descriptions of the LMMs and their sizes can be found in Appendix B.2.

**Datasets:** To evaluate performance across diverse scenarios, we conducted experiments using two datasets. The first was a synthetic workload, that allowed setting custom parameters such as prompt length, number of images per request, image resolution, output length, and sampling settings. Unless otherwise specified in our experiments, the input prompt length was set to 22 tokens. The second dataset was NextQA [18], a benchmark video question-answering dataset. Unlike synthetic workload, NextQA features human-annotated questions and answers, providing a more realistic reflection of real-world video request distributions.

**Evaluation Metrics:** We evaluate the system based on runtime performance and memory consumption. The related performance metrics are listed below.

- **TTFT:** The time from the submission of a request to the system until the first token is received by the user.
- **TPOT:** The average time interval between each output token (excluding the first token).
- **SLO Attainment:** The percentage of requests that meet predefined SLOs, such as TTFT and TPOT requirements.
- **Goodput:** The highest request rate at which 90% or more SLO attainment is achieved.

For memory benchmarking experiments, we analyze the baselines by evaluating the benefits of available free mem-

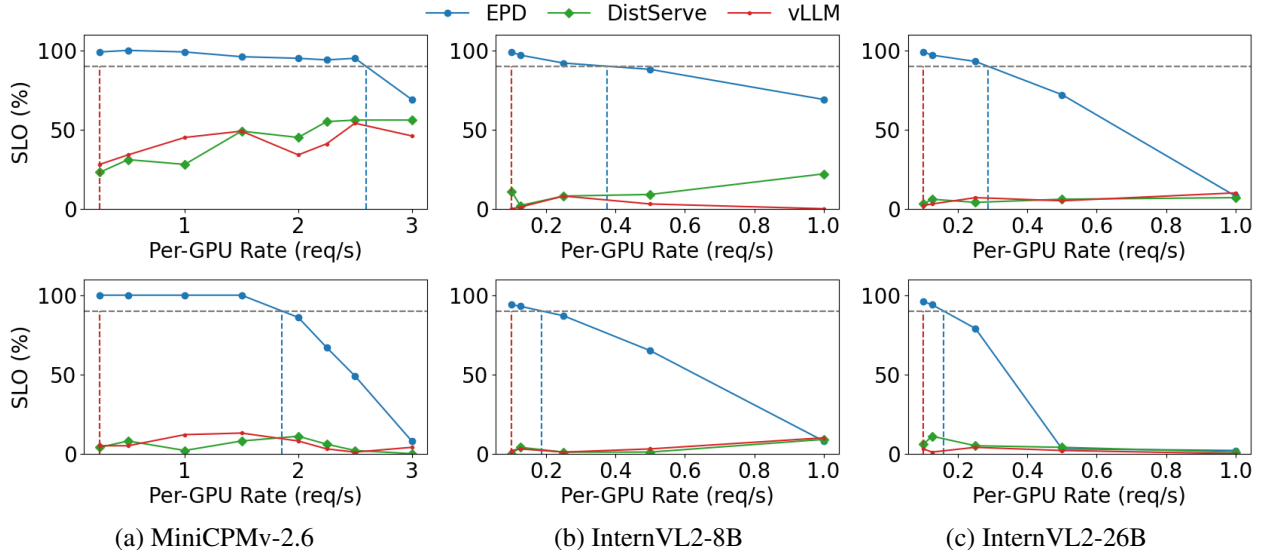


Figure 5. SLO attainment for end-to-end inference across various models and image counts per request. Columns (a), (b), and (c) correspond to the MiniCPM-V 2.6, InternVL2-8B, and InternVL2-26B, respectively. The top and bottom rows are with 2 and 4 images per request, respectively. As observed, EPD significantly outperforms all baselines across all configurations.

ory. Additional free memory can facilitate higher batch sizes, accommodate more images per request, or enable larger key-value (KV) cache sizes. (See section 4.3)

#### 4.1. SLO Attainment for End-to-End Generation

In this experiment, we evaluate the goodput of EPD and the baselines in an online setting, where 100 multimodal requests arrive following a Poisson process with rate  $\lambda$ . The length of output tokens is fixed to 10. We test requests with 2 and 4 images, each at a resolution of  $4032 \times 3024$ . The details of the corresponding SLO criteria are discussed in appendix B.3. The results for three models (columns) are presented in Fig. 5. The X-axis represents the per-GPU request rate ( $\lambda/\#$ GPUs), and the Y-axis indicates the percentage of requests meeting both TTFT and TPOT requirements, with a 90% threshold denoted by a black dotted line.

EPD outperforms all baselines, achieving over 90% SLO attainment at lower request rates. This is due to its ability to parallelize the computationally intensive image encoding step across multiple GPUs. DistServe and vLLM often maintain less than 10% attainment due to interference. Meanwhile, comparing the first and second rows for varying image counts per request (2 and 4), we observe that while more images per request increase workload, EPD maintains reasonable performance, whereas baseline SLO attainment drops significantly. Lastly, InternVL, being prefill-heavy, experiences queuing delays due to the higher number of image tokens, particularly at higher request rates. This effect exacerbates performance degradation from the 8B to the 26B model. In contrast, MiniCPM-V, optimized to gen-

erate fewer image tokens, avoids these delays and achieves better overall latency. Further, we provide more results with 6 and 8 images in Appendix D.1.

Next, we repeat the experiment using the non-synthetic video question-answering dataset, NextQA [18]. For this, we randomly sampled 100 examples, with input text token lengths ranging from 4 to 21 (average: 11.42) and output token lengths ranging from 1 to 7 (average: 2.75). Each video request was represented by 8 uniformly sampled frames, and we used MiniCPM-V 2.6 in the experiment, adhering to the SLO criteria of TTFT = 5.60 and TPOT = 0.06. As illustrated in Fig. 7, EPD is the only framework achieving 90% SLO attainment at low request rates, demonstrating its superior effectiveness in handling diverse, real-world-like workloads compared to DistServe and vLLM.

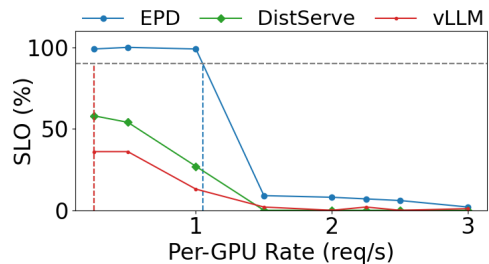


Figure 7. SLO attainment for end-to-end inference on the NextQA dataset. As seen, EPD outperforms other baselines by a significant margin.

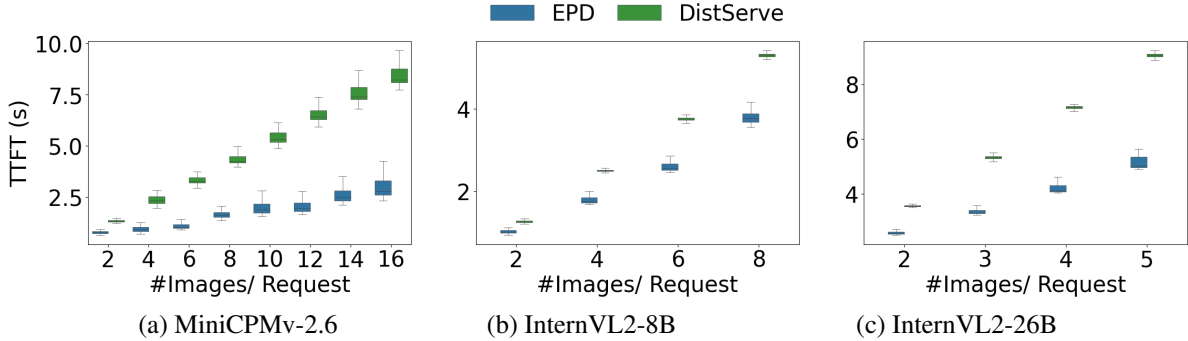


Figure 6. Distribution of TTFT (Y-axis) for various #Images/ Request (X-axis) for the MiniCPM-V 2.6 (left), InternVL2-8B (middle), and InternVL2-26B (right)

## 4.2. First Token Generation Latency

Multimodal requests often place a heavy load on both the E and P phases, making the first token generation a key latency bottleneck. Therefore, in this experiment, we analyze the first token latency for various baselines. The results presented in Fig. 6 shows box plots of TTFT distributions for three different models. Note that, as the decoding phase is excluded, the vLLM baseline is equivalent to DistServe and is thus skipped. Requests are generated according to a Poisson distribution with a fixed request rate  $\lambda$ . Specifically,  $\lambda = 0.25$  for the MiniCPM-V 2.6, and  $\lambda = 0.08$  for both the InternVL2-8B and InternVL2-26B. Thanks to intra-request parallelization, EPD significantly outperforms both baselines, EPD and DistServe. Specifically, TTFT is reduced by up to 71.9%, 32.8%, and 44.9% compared to the DistServe baseline for the MiniCPM-V 2.6, InternVL2-8B, and InternVL2-26B models, respectively. The performance gain grows with the number of images per request, demonstrating EPD’s efficiency in handling heavy multimodal workloads.

## 4.3. Memory Savings through Stage Disaggregation

In this section we analyze the memory savings achieved by disaggregating the encoding and prefill stages. The E workers can save memory as they do not require LLM weights or the KV cache. Analyzing only the weight size indicates memory reduction of approximately 95%, 96.2%, and 78.3% for the MiniCPM-V 2.6, InternVL2-8B, and InternVL2-26B models. Similarly, for the P workers, memory saving of about 5%, 3.7%, and 21.6% are achieved, respectively. In practice, since KV cache is also not required at E workers, the memory saving can be even higher (93.3% saving, i.e.,  $15\times$  lower, according to profiling). These reductions in memory usage enable the EPD system to support higher numbers of images per request and batch sizes (discussed in the following experiments) and larger KV cache sizes (discussed in Appendix D.2).

### EPD Supports a Higher Number of Images per Re-

Model	Image Reso.	DistServe	EPD
MiniCPM-V 2.6	313,234	77	<i>490</i>
	787,444	26	<i>165</i>
	4032,3024	7	<i>49</i>
InternVL2-8B	313,234	19	19
	787,444	19	19
	4032,3024	19	19
InternVL2-26B	313,234	1	<i>10</i>
	787,444	11	<i>45</i>
	4032,3024	1	<i>10</i>

Table 1. Comparison of maximum supported number of images/request. Batch size is fixed to 1. KV cache is allocated as 80% of the available free memory. Higher (*italicized*) is better.

**quest:** We compare the maximum number of images per request supported by the disaggregated (EPD) and aggregated (DistServe or vLLM) systems across three multimodal models: MiniCPMv, InternVL2-8B, and InternVL2-26B. The experiment was conducted at three different image resolutions, with a fixed batch size of 1 and with 80% of the available memory allocated for KV cache. As shown in Tab. 1, EPD handles more images per request than DistServe, for example, at  $4032\times 3024$  resolution,  $7\times$  more for InternVL2-26B and  $10\times$  more for InternVL2-8B. For InternVL2-8B, the limit of 19 images per request is due to its maximum context length. Without this constraint, a larger number of images per request could be supported.

**EPD Supports Higher Batch Sizes:** We compare maximum supported batch sizes for E and P stages across different settings of image resolution and models in Tab. 2. As seen, EPD significantly outperforms DistServe for both E and P batch sizes. For example, with InternVL2-26B at  $787\times 444$  resolution, EPD supports a batch size of 22 for encoding vs. DistServe’s 1, achieving  $22\times$  improvement. Similarly, for MiniCPM-V 2.6 at  $787\times 444$ , EPD achieves a batch size of 29 vs. DistServe’s 2 for prefill, a  $14.5\times$  im-

provement.

Model	Image Reso.	#Patch	DistServe (E, P)	EPD	
				E	P
MiniCPMv 2.6	313,234	1	7	<i>49</i>	<i>86</i>
	787,444	3	2	<i>16</i>	<i>29</i>
	4032,3024	10	OOM	4	9
InternVL2-8B	313,234	13	2	<i>15</i>	2
	787,444	3	9	<i>67</i>	<i>10</i>
	4032,3024	13	2	<i>15</i>	2
InternVL2-26B	313,234	13	OOM	6	1
	787,444	3	1	22	4
	4032, 3024	13	OOM	6	1

Table 2. Comparison of maximum supported E and P batch size. #images/ request is fixed to 10. KV cache is allocated as 80% of the available free memory. Higher (*italicized*) is better.

#### 4.4. Ablation Study

In this section, we analyze the impact of various components of the proposed system.

	#I/R=2	#I/R=4	#I/R=6	#I/R=8
EPD	0.92	1.02	1.14	1.74
w/o IRP	1.46 ( <b>1.6x</b> )	2.47 ( <b>2.4x</b> )	3.37 ( <b>2.9x</b> )	4.27 ( <b>2.5x</b> )

Table 3. Effect of ablating IRP feature from the proposed system on TTFT (s). Disabling IRP negatively affects the TTFT (up to 2.9x worse) for various multiple images/ request (#I/R). Results are averaged over 100 requests.

**Effect of IRP:** We analyze the effect of ablating IRP, presented in Section 3.2.2. The experimental settings are same as TTFT experiment in Sec. 4.2. As shown in Tab. 3, removing the IRP feature negatively affects TTFT across various images/ request. Moreover, the degradation exacerbates as the number of images/ request increases. This is because the IRP feature allows parallelization of encoding load within the same request across multiple GPUs.

	Goodput (r/s) ↑	TTFT (s) ↓	TPOT (s) ↓
EDP	1.25	2.12	0.031
w/o Opt.	0.56 ( <b>2.2x</b> )	4.48 ( <b>2.1x</b> )	0.025 ( <b>0.8x</b> )

Table 4. Effect of Offline Optimizer. When the configuration is set randomly, the goodput is 2.2x worse on average. ↓ indicates that lower is better and ↑ means that larger is better.

**Effect of Offline Optimizer:** By default, the EPD system collects workload samples and finds the optimal config offline using the optimizer. To demonstrate its effect, we conduct an experiment without using the optimizer and set configs randomly. Specifically, we uniformly sample 10 configs at random and report the estimated expectation of

the performance metric in the second row of Tab. 4. For a fair comparison, when evaluating the TTFT and TPOT, we maintain the same request rate of 1.25 r/s, which is the goodput of the EPD system. (See Appendix B.4 for more details) As shown in Tab. 4, disabling the optimizer causes significant performance degradation, in terms of both goodput and TTFT. This demonstrates the necessity of the optimizer, especially when the EPD system has many tunable configs.

**Effect of Dynamic Role Switching:** To analyze the impact of dynamic role switching, we conduct a controlled experiment simulating a shift in workload characteristics. Specifically, we generate 100 requests following the same static workload configuration as described in Section 3.2.4. However, to introduce an artificial workload change, we set the first 10 requests to generate 50 output tokens, while the remaining 90 requests generate 500 output tokens. The request arrival rate is fixed at 3 requests per second. The results are shown in Tab. 5.

	Latency (s) ↓	TTFT (s) ↓	TPOT (s) ↓
EPD	28.01	1.42	0.05
w/o Switch	61.10 ( <b>2.2x</b> )	1.33 ( <b>0.9x</b> )	0.12 ( <b>2.4x</b> )

Table 5. Effect of ablating dynamic role switching feature from EPD. Disabling the worker migration feature negatively affects the TPOT (2.4x worse), which results in significantly poor end-to-end latency (2.2x worse). Results are averaged over 100 requests with one 4K image per request. ↓ indicates that lower is better.

Without dynamic worker migration, the system performs poorly because it remains locked in the initial configuration (5E1P2D, optimized offline for 50 tokens) and is unable to adapt to the increased decoding demand. In contrast, the EPD system with migration dynamically reconfigures itself (2E1P5D) to handle the new workload (500 output tokens) by shifting 3 E instances to D, resulting in approximately 2x better performance.

#### 4.5. Adaptation to Neural Processing Units (NPUs)

This section presents the results of adapting the proposed EPD framework to Huawei Ascend NPUs. For more details on the implementation and experiments, see Appendix B.5.

First, we compare the EPD-NPU against the vLLM and DistServe baselines in terms of SLO attainment using the InternVL2-8B LMM. We used the same settings as mentioned in Sec. 4.1, except that we used a heavy encoding workload of 8 4032x3024 images per request. The optimal configuration for this workload was found to be 5E2P1D and the corresponding results are presented in Figure 8. As seen, EPD is the only setting that can achieve the SLO requirements, while the other baselines are completely decimated even for low request rates.

Next, we compare the TTFT of EPD-NPU against



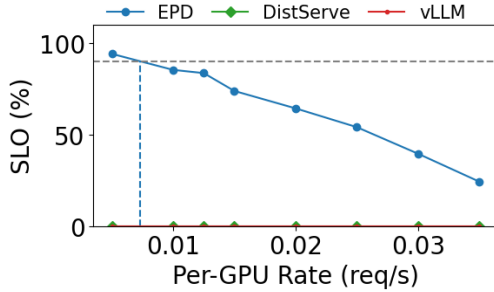


Figure 8. SLO curve for InternVL2-8B with the following requirements (TTFT=8.5 and TPOT=0.12) on the controlled experimental setup with 8 images per request.

vLLM. We found that EPD-NPU demonstrated a 35.2% improvement over vLLM, which is significantly more than the 24.4% improvement for the GPU scenario. We attribute this additional  $\sim 10\%$  to the proportionally heavier encode of LLMs on NPU compared to GPU. Please refer to Appendix D.3 for more details. This results in greater benefits of disaggregating the encode from prefill on NPU in comparison to GPU.

## 5. Conclusion

In this paper, we present a novel approach to optimizing Large Multimodal Model (LMM) systems through the disaggregation of key processing stages. By separating the encoding, prefill, and decoding tasks into distinct stages, our system offers enhanced flexibility in resource allocation, enabling more efficient management of computational and memory resources. This disaggregation, combined with dynamic resource allocation, asynchronous token transfer, and advanced parallelization strategies, directly addresses several critical challenges in LMM deployment, including latency reduction, memory optimization, and efficient computational resource usage.

## References

- [1] Josh Achiam, Steven Adler, Sandhini Agarwal, Lama Ahmad, Ilge Akkaya, Florencia Leoni Aleman, Diogo Almeida, Janko Altenschmidt, Sam Altman, Shyamal Anadkat, et al. Gpt-4 technical report. [arXiv:2303.08774](https://arxiv.org/abs/2303.08774), 2023. 1
- [2] Amey Agrawal, Ashish Panwar, Jayashree Mohan, Nipun Kwatra, Bhargav S. Gulavani, and Ramachandran Ramjee. Sarathi: Efficient llm inference by piggybacking decodes with chunked prefills. [arXiv:2308.16369](https://arxiv.org/abs/2308.16369), 2023. 2
- [3] Borja Calvo, Ofer M Shir, Josu Ceberio, Carola Doerr, Hao Wang, Thomas Bäck, and Jose A Lozano. Bayesian performance analysis for black-box optimization benchmarking. In *Proceedings of the Genetic and Evolutionary Computation Conference Companion*, pages 1789–1797, 2019. 5
- [4] Yupeng Chang, Xu Wang, Jindong Wang, Yuan Wu, Linyi Yang, Kaijie Zhu, Hao Chen, Xiaoyuan Yi, Cunxiang Wang, Yidong Wang, et al. A survey on evaluation of large language models. *ACM Transactions on Intelligent Systems and Technology*, 15(3):1–45, 2024. 1
- [5] Z. Chen, J. Wu, W. Wang, W. Su, G. Chen, S. Xing, M. Zhong, Q. Zhang, X. Zhu, L. Lu, B. Li, P. Luo, T. Lu, Y. Qiao, and J. Dai. Internvl: Scaling up vision foundation models and aligning for generic visual-linguistic tasks. In *Proceedings of CVPR*, pages 24185–24198, 2024. 1, 5
- [6] Cunchen Hu, Heyang Huang, Liangliang Xu, Xusheng Chen, Jiang Xu, Shuang Chen, Hao Feng, Chenxi Wang, Sa Wang, Yungang Bao, et al. Inference without interference: Disaggregate llm inference for mixed downstream workloads. [arXiv:2401.11181](https://arxiv.org/abs/2401.11181), 2024. 2
- [7] Yibo Jin, Tao Wang, Huimin Lin, Mingyang Song, Peiyang Li, Yipeng Ma, Yicheng Shan, Zhengfan Yuan, Cailong Li, Yajing Sun, et al. P/d-serve: Serving disaggregated large language model at scale. [arXiv:2408.08147](https://arxiv.org/abs/2408.08147), 2024. 2, 3
- [8] Hao Kang, Qingru Zhang, Souvik Kundu, Geonhwa Jeong, Zaoxing Liu, Tushar Krishna, and Tuo Zhao. Gear: An efficient kv cache compression recipe for near-lossless generative inference of llm. [arXiv:2403.05527](https://arxiv.org/abs/2403.05527), 2024. 2
- [9] Woosuk Kwon, Zhuohan Li, Siyuan Zhuang, Ying Sheng, Lianmin Zheng, Cody Hao Yu, Joseph E. Gonzalez, Hao Zhang, and Ion Stoica. Efficient memory management for large language model serving with paged attention. In *Proceedings of the ACM SIGOPS 29th Symposium on Operating Systems Principles*, 2023. 2, 5
- [10] Yuhong Li, Yingbing Huang, Bowen Yang, Bharat Venkitesh, Acyr Locatelli, Hanchen Ye, Tianle Cai, Patrick Lewis, and Deming Chen. Snapkv: LLM knows what you are looking for before generation. [arXiv:2404.14469](https://arxiv.org/abs/2404.14469), 2024. 2
- [11] Haotian Liu, Chunyuan Li, Qingyang Wu, and Yong Jae Lee. Visual instruction tuning. In *Proceedings of NeurIPS*, 2023. 1
- [12] Huan Liu, Yujie Zhang, Xue Yang, Xiaowei Li, Huan Chen, Jure Zhu, and Yu Gong. A survey of resource-efficient llm and multimodal foundation models. [arXiv:2401.08092](https://arxiv.org/abs/2401.08092), 2024. 1
- [13] Zhenyu Ning, Jieru Zhao, Qihao Jin, Wenchao Ding, and Minyi Guo. Inf-mllm: Efficient streaming inference of multimodal large language models on a single gpu. [arXiv:2409.09086](https://arxiv.org/abs/2409.09086), 2024. 2, 3
- [14] Pratyush Patel, Esha Choukse, Chaojie Zhang, Aashaka Shah, Inigo Goiri, Saeed Maleki, and Ricardo Bianchini. Splitwise: Efficient generative llm inference using phase splitting. In *2024 ACM/IEEE 51st Annual International Symposium on Computer Architecture (ISCA)*, pages 118–132, 2024. 2, 3
- [15] Ruoyu Qin, Zheming Li, Weiran He, Mingxing Zhang, Yongwei Wu, Weimin Zheng, and Xinran Xu. Mooncake: A kv-cache-centric disaggregated architecture for llm serving. [arXiv:2407.00079](https://arxiv.org/abs/2407.00079), 2024. 2, 3
- [16] Foteini Strati, Sara McAllister, Amar Phanishayee, Jakub Tarnawski, and Ana Klimovic. Déjàvu: Kv-cache streaming for fast, fault-tolerant generative llm serving. In *ICML*, 2024. 3
- [17] Jiayang Wu, Wensheng Gan, Zefeng Chen, Shicheng Wan, and S Yu Philip. Multimodal large language models: A sur-

- vey. In 2023 IEEE International Conference on Big Data (BigData), pages 2247–2256. IEEE, 2023. [1](#)
- [18] Junbin Xiao, Xindi Shang, Angela Yao, and Tat-Seng Chua. Next-qa: Next phase of question-answering to explaining temporal actions. In Proceedings of the IEEE/CVF Conference on Computer Vision and Pattern Recognition (CVPR), pages 9777–9786, 2021. [5](#), [6](#)
- [19] Yuan Yao, Tianyu Yu, Ao Zhang, Chongyi Wang, Junbo Cui, Hongji Zhu, Tianchi Cai, Haoyu Li, Weilin Zhao, Zhihui He, et al. Minicpm-v: A gpt-4v level mllm on your phone. arXiv:2408.01800, 2024. [1](#), [5](#), [12](#)
- [20] Gyeong-In Yu, Joo Seong Jeong, Geon-Woo Kim, Soojeong Kim, and Byung-Gon Chun. Orca: A distributed serving system for Transformer-Based generative models. In 16th USENIX Symposium on Operating Systems Design and Implementation (OSDI 22), pages 521–538, 2022. [2](#)
- [21] Yinmin Zhong, Shengyu Liu, Junda Chen, Jianbo Hu, Yibo Zhu, Xuanzhe Liu, Xin Jin, and Hao Zhang. Distserve: Disaggregating prefill and decoding for goodput-optimized large language model serving. In OSDI, pages 193–210. USENIX Association, 2024. [2](#), [3](#), [4](#), [5](#), [11](#)

## A. Optimizer Details

We recapitulate the configuration optimization problem:

$$\max_{(\mathbf{p}, \mathbf{b}, \mathbf{s}) \in \mathcal{X}} f(\mathbf{p}, \mathbf{b}, \mathbf{s}) - \beta \cdot \text{cost}(\mathbf{p}) \quad (2)$$

For the search space  $\mathcal{X}$ , there could be implicit constraints during the configuration search. For example, the total number of GPUs must not exceed the available resources (e.g., 8 or 16). Alternatively, if the cloud service provider intends to fully utilize all available 8 GPUs, an implicit constraint could enforce the number of GPUs to be exactly 8. These constraints serve to reduce the search space. The system configuration involves parallelization configurations  $\mathbf{p}$ , maximum batch size configurations  $\mathbf{b}$ , and scheduling configurations  $\mathbf{s}$ . These variables are vectors, where each element corresponds to the configuration of an individual instance. Each instance is capable of handling requests independently, including managing (sub-)workers for tensor parallelism and pipeline parallelism. Instances within a stage process different requests in parallel, a concept referred to as data parallelism. Note that  $\mathbf{p}$ ,  $\mathbf{b}$ , and  $\mathbf{s}$  can have variable lengths, as the number of instances is itself a configurable parameter. For the  $i$ -th instance, we denote its stage as  $\text{Stage}_i \in \{E, P, D\}$ , where  $E$  represents the encoder stage,  $P$  represents the processing stage, and  $D$  represents the decoder stage.

- **Parallelization:** Let  $\mathbf{p}$  denote the vector of parallel configs for all instances. For the  $i$ -th instance, if it is a prefill or decoding instance, then its config  $p_i$  includes:  $p_i^{\text{TP}}$ , the number of GPUs used for tensor parallelism; and  $p_i^{\text{PP}}$ , the number of GPUs used for pipeline parallelism. If it is an encoding instance, considering IRP does not require communication, which is better than TP, we only use IRP. Therefore for encode, we overload the symbol  $p_i^{\text{TP}} = p_i^{\text{IRP}}$  to denote the number of GPUs used for IRP. If the cost per GPU is a constant  $c$ , then the total cost is:  $\text{cost}(\mathbf{p}) = c \sum_{p_i \in \mathbf{p}} (p_i^{\text{TP}} \times p_i^{\text{PP}})$ .
- **Max Batch Size** determines how many requests are processed simultaneously during the encoding, prefill, and decoding stages. Let  $\mathbf{b}$  denote the batch size config for all instances. For  $i$ -th instance,  $b_i$  is its max batch size. This config involves a trade-off between latency and throughput. Larger batch sizes improve throughput by enabling parallel processing but may increase latency if the stages become compute-bound.
- **Scheduling** involves two main decisions: First, which workers should each request be assigned to? Second, how should the order of requests be determined within a worker queue? To solve these decisions, we adapt strategies from the DistServe framework [21]. In the encoding stage, when a request arrives, it is assigned and pushed to an instance queue. Between different stages, global queues are used, and each available engine pulls proactively from the queues. Possible assignment strategies in the encoding stage include Round-Robin or Least-Loaded First for assigning requests. Once a request is assigned to a worker’s queue, we can apply ordering strategies like first-come-first-serve or shortest-job-first, or more complex strategies that prioritize requests based on their Service Level Objectives (SLOs). For simplicity, we constrain that all instances within the same stage share the same scheduling strategy.

## B. Implementation Details

EPD is a fully capable distributed serving system for LMMs, comprising several key components: a load estimation module, a resource allocation module, a RESTful API frontend, and a multimodal-aware orchestration layer. The entire framework is implemented with a mix of Python and C++/ CUDA implementations, ensuring superior scalability and performance. To facilitate integration, we repurpose the distributed execution engine from vLLM, which supports numerous popular LLMs and LMMs, allowing easy adaptation of new models into our disaggregated framework with minimal effort.

The API interface adheres to OpenAI’s multimodal specifications, enabling users to specify parameters such as output length, temperature, and multimodal data inputs.

The scheduler is specifically designed for the disaggregated EPD framework, dynamically managing batch sizes and enabling asynchronous execution of the encoding, prefill, and decoding phases. The load estimation module ensures efficient GPU allocation across these phases, adapting to changing workload demands in real time.

Our repurposed distributed execution engine uses Ray actors to implement GPU workers, which manage multimodal and key-value caches, and coordinate the independent execution of the encoding, prefill, and decoding tasks. Furthermore, it supports 3D parallelism, incorporating Data Parallelism (DP), Tensor Parallelism (TP), and Pipeline Parallelism (PP) to maximize resource utilization and scalability.

The orchestration layer includes custom CUDA kernels optimized for parallelism in the encoding and prefill phases. These kernels enable efficient management of paged multimodal caches and ensure seamless asynchronous transfer of multimodal tokens between encoding and prefill GPUs. The orchestration layer oversees the execution of encoding, prefill, and decoding instances, handling tasks such as request distribution, KV cache transmission, and result aggregation. For efficient data

movement, the system employs NCCL for inter-node GPU communication and asynchronous `CudaMemcpy` for intra-node transfers, ensuring smooth operations without disrupting GPU computations across the disaggregated EPD framework.

### B.1. Hyper-parameters in EPD system

We conducted our experiments using a cluster of 8 NVIDIA A100 GPUs (82GB). Each server was equipped with 128 CPUs and 1TB of RAM. The CUDA version was 12.2. Flash attention-2 was used for the attention implementation. We use FP16 precision for all experiments.

To ensure a fair comparison, we standardized key performance-affecting settings of the inference engine across all baselines. Specifically, these include a block size of 16; a maximum of 2048 blocks per request; context tokens capped at 49,152, and decoding tokens at 81,920 per batch. The scheduling policy for all stages was set to First-Come-First-Served (FCFS). Further, to allow enough resources for memory-heavy multimodal requests to execute, KV cache GPU utilization was set to 50%, and the maximum number of multimedia data of 32 was imposed per prompt. The size of the multimodal cache was fixed to 3000 across all models, and the vLLM inference engine was run in eager mode. Finally, for the vLLM inference engine, we used the version 0.6.1.post1 which represents a stable version for multimodal inference.

In our online experiments, requests were sent to the inference engine using a Poisson arrival process with a fixed  $\lambda$ , representing the number of requests per second. Each trial was executed until 100 requests were completed, ensuring sufficient data for consistent performance analysis. Further, to optimize TTFT and TPOT in this latency-sensitive setting, we disabled batching by setting batch sizes to 1 for the encoding, prefill, and decoding stages.

### B.2. LMM Details

MiniCPM-V 2.6 integrates a SigLip-400M vision encoder, comprising 400 million parameters, with a Qwen2-7B language model, containing 7.6 billion parameters, culminating in 8 billion parameters. It excels in tasks involving single-image, multi-image, and video comprehension, even surpassing GPT-4V in these domains [19].

InternVL2-8B features an InternViT-300M-448px vision encoder with 300 million parameters, paired with an internlm2\_5-7b-chat language model comprising 7.7 billion parameters, totaling 8 billion parameters. Similarly, InternVL2-26B combines an InternViT-6B-448px-V1-5 vision encoder with 6 billion parameters and an internlm2-chat-20b language model containing 20 billion parameters, resulting in 26 billion parameters.

### B.3. SLO Criteria

Tab. 6 outlines the SLO criteria for TTFT and TPOT across various models and different numbers of images per request (#I/R). These criteria are empirically derived based on the characteristics of the underlying models, such as the computational complexity of the MME and LLM. We also consider what is realistically achievable by both our method and the baselines on a fixed number (8 GPUs) used in experiments. Across models, as #I/R increases, there is an approximately linear increase in the TTFT criteria due to the higher encoding load and additional tokens generated during the prefill stage. In contrast, TPOT requires only minor adjustments since it is not directly impacted by changes in #I/R.

#I/R	MiniCPMv 2.6 8B		InternVL 8B		InternVL 26B	
	TTFT	TPOT	TTFT	TPOT	TTFT	TPOT
2	1.40	0.04	1.20	0.05	3.50	0.07
4	2.60	0.04	2.40	0.06	7.05	0.08
6	3.90	0.06	3.55	0.09	11.00	0.95
8	5.10	0.06	5.00	0.18	15.00	0.15

Table 6. Requirements for TTFT and TPOT (in seconds) used for SLO computation across various models and number of images per request (#I/R) in the experiments.

### B.4. Details for the Ablation Experiment of Offline Optimizer

In this experiment, 100 User requests arrive in real-time with each request containing 6 images, and they all request for the MiniCPMv model. For simplicity, we limit the configuration space to a restricted search space, where each data-parallel (DP) worker uses the same batch size configuration, and both TP and PP are fixed to 1. We explore the batch size configurations for workers across different stages, the number of DP workers in each stage, and the decision to enable IRP. The config identified by the optimizer is as follows: batch sizes for the E, P, and D stages are 2, 1, and 128, respectively; the number of workers in each stage is 6, 1, and 1; and IRP is enabled. We uniformly random-sample 10 configs from the search space.

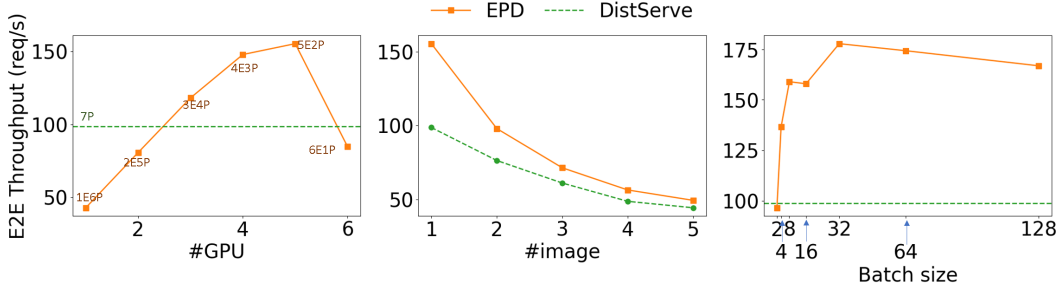


Figure 9. **Left:** The impact of tuning the number of encoding workers in the EPD method. The annotation ‘xEP’ indicates that x encoders and y prefill workers are allocated for EPD, and ‘7P’ means that the DistServe always allocates 7 P workers for the encoding and prefill stage requests. **Middle:** The impact of the number of images per request in the workload. **Right:** The impact of encoding and prefill batch sizes in the EPD method (encoding and prefill batch sizes are set to be equal).

To maintain the same computational cost, all 8 GPUs are utilized across different configs. Consequently, the search space is constrained to leverage 8 GPUs, which can be enforced through rejection sampling. The sample mean of the performance metric (goodput, TTFT, and TPOT) is presented in Table 4. Recall that the goodput metric is defined as the maximum request rate while maintaining an SLO attainment of no less than 90%. For a fair comparison, When evaluating the TTFT and TPOT, we maintain the same request rate of 1.25 r/s, which is same as the goodput of the EPD system.

## B.5. NPU Implementation Details

There are intrinsic differences between NPU and GPU architectures and processing characteristics. GPUs are general-purpose compute resources whereas NPUs have been specifically designed for neural networks. NPUs are optimized for FP16 calculations whereas GPUs are optimized for FP32 calculations. As stated above, CANN operators are used on Ascend NPU hardware in place of CUDA operators. These differences between CUDA and corresponding CANN operators, having been optimized for the hardware they are built upon, result in different latencies and trade-offs in inference as well as communication between NPU/GPU chips. This results in different encode/prefill/decode latencies which may be present different benefits from EPD and IRP.

The EPD-NPU system was implemented in a similar manner to our EPD-GPU system as described in Appendix B. All EPD-NPU experiments utilize IRP. The EPD-NPU distributed serving system was developed and deployed on a cluster of 910B3 NPUs, each with 64GB of high bandwidth memory. Some primary differences between the two implementations include:

- **Ascend-vLLM:** EPD-NPU leverages Ascend-vLLM rather than vLLM which is an adaptation of vLLM on Ascend NPU hardware that utilizes the Compute Architecture for Neural Networks (CANN) software stack rather than CUDA.
- **Container-based deployment:** Each encode, prefill, and decode instance is deployed separately as an API for the scheduler engine to call. These instances run in data parallel mode. The scheduler engine simply sends a POST request to the corresponding API with some minimal request-specific information (e.g., request ID, sampling parameters, block IDs to pull) and the remaining implementation mirrors that of EPD-GPU. This container-based deployment allows our framework to be easily scalable and portable to the cloud, providing intriguing future works regarding efficient utilization and scheduling of resources for users.

These differences in characteristics provide an opportunity to investigate the generalizability of our EPD framework and further understand the optimal setting/environment for disaggregating encode and prefill.

For EPD-NPU, we use eight 910B3 NPUs and evaluate the system by running the controlled experimental setup (as described in the experiments section of the main paper) in an online setting. Specifically, the number of input tokens was 22, length of output tokens was 10 with early stopping was disabled. The SLO requirements were also selected in a similar manner as the GPU experiments. The requirements for InternVL2-8B with 8 images per request were 8.5 and 0.12 for TTFT and TPOT, respectively. Each server had 192 CPUs and 1.5TB of RAM. The CANN version was 7.6. The maximum model length was set to 27000, KV Cache utilization was set to 83% And the maximum number of multimedia data of 8 was imposed. EPD-NPU also used a version of Ascend-vLLM (version 0.6.3.post1) built upon a newer version of vLLM than the one used in EPD-GPU. Unless otherwise stated, the hyper-parameters are identical to those described in B.1.

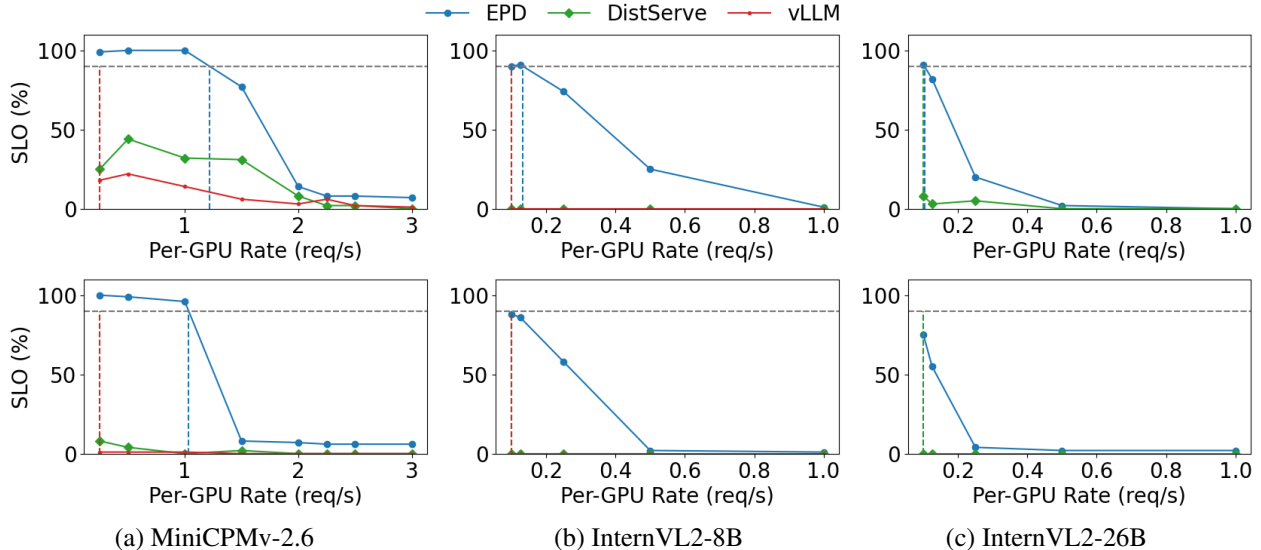


Figure 10. Columns (a), (b), and (c) correspond to MiniCPM-V 2.6, InternVL2-8B, and InternVL2-26B, respectively. The top and bottom rows show results for 6 and 8 images per request, respectively. As expected, EPD maintains a significant performance advantage over all baselines, demonstrating robustness of the system as the image count increases.

### C. Throughput in Offline Settings

In this section, we demonstrate the benefits of the EPD method in terms of throughput, specifically focusing on its memory efficiency and the ability to support higher batch sizes for both the E and P stages.

Consider an offline scenario where a batch of requests is submitted, allowing the system to process them overnight with a focus on maximizing end-to-end (E2E) throughput. This is an additional performance metric complementing the main body of the paper, measured in terms of requests completed per second and the system’s ability to handle high request volumes in offline settings. In the traditional DistServe method, memory is allocated for both the encoding and prefill stages on the same worker, which is constrained by the total memory capacity of the GPU.

This memory limitation becomes especially significant in heterogeneous environments with low-end GPUs that have limited memory. In these cases, the DistServe method struggles to fully utilize low-end GPUs, as the combined memory demands of the encoding and prefill stages exceed the available memory. In contrast, our disaggregated EPD method is more cost-effective, as it assigns the low-end GPUs exclusively to the encoding stage, allowing better utilization of available memory. In this experiment, we consider a less extreme scenario where the memory demands of the prefill workers in the DistServe method do not exceed the memory capacity of the low-end GPUs, allowing for a batch size of 1 for both the encoding and prefill stages.

We use 8 A800 GPUs for this experiment. For EPD, we allocate 5 GPUs for encoding (E), 2 GPUs for prefill (P), and 1 GPU for decoding (D), with the maximum batch sizes set to 8, 8, and 128 for E, P, and D, respectively. In the DistServe method, we allocate 7 GPUs for prefill (P) and 1 GPU for decoding (D), with the maximum batch sizes of 1 and 128, respectively. The workload consists of 1,000 requests, each with a single image, a simple prompt (“What is the content of this image?”), and a maximum of 10 output tokens. We tune the system’s hyperparameters as outlined in Sec. 3.2.3 and evaluate their impact on throughput. The results are presented in Fig. 9.

The left plot illustrates the importance of selecting an appropriate GPU configuration. As described in Sec. 3.2.3, our algorithm automatically identifies that a 5E2P configuration (5 encoder and 2 prefill workers) maximizes E2E throughput. The middle plot shows that EPD achieves superior throughput when the number of images per request is low, demonstrating that EPD’s architecture prevents the encoder from becoming a compute-bound bottleneck. The right plot highlights that EPD’s performance is relatively insensitive to encoding and decoding batch sizes, consistently outperforming the DistServe method. This flexibility allows us to either choose a relatively large batch size or rely on the algorithm in Sec. 3.2.3 to automatically select an optimal batch size.

Model	# Images/Req.	DistServe	EPD
MiniCPM-V 2.6	5	86%	99%
	10	74%	97%
	20	49%	95%
	40	OOM	92%
	80	OOM	OOCL
InternVL2-8B	5	94%	95%
	10	89%	91%
	20	OOCL	OOCL
InternVL2-26B	5	67%	89%
	10	36%	80%
	20	OOM	63%
	40	OOM	OOCL

Table 7. Comparison of maximum supported KV cache size (in terms of percentage of free memory) on prefill node for various #images/request. Image resolution fixed to 4K. Higher (*italicized*) is better.

## D. Additional Experiments

### D.1. SLO Attainment for End-to-End Generation for 6 and 8 images

In this section, we show additional results from the experiment in Sec. 4.1 pertaining to 6 and 8 images per request. As seen, the SLO attainment for EPD begins to decline as number of images rise, particularly at higher request rates. This decline reflects the increasing computational demand associated with processing multiple high-resolution images within a single request. Nevertheless, EPD continues to outperform all baselines, which struggle even at low request rates and fail to scale effectively under increased workloads.

### D.2. EPD Supports Larger KV Cache Sizes:

We compare the maximum KV cache size that can be allocated across systems. The batch size is fixed at 1, and the image resolution is set to  $4032 \times 3024$ . As shown in Tab. 7, EPD supports significantly larger KV cache sizes than DistServe. For instance, for the InternVL2-26B model at 10 images per request, EPD can support a KV cache size of 80% vs 36% for DistServe, representing a  $2.2 \times$  improvement. Notably, in certain scenarios—such as with the InternVL2-26B model and 20 images per request—the DistServe system encounters an OOM error, indicating that it cannot process 20 images even with a KV cache size of 0. Additionally, some configurations encounter an Out of Context Limit (OOCL) error, where the large number of encoding tokens generated by high image counts exceeds the LLM’s context limit during the prefill stage.

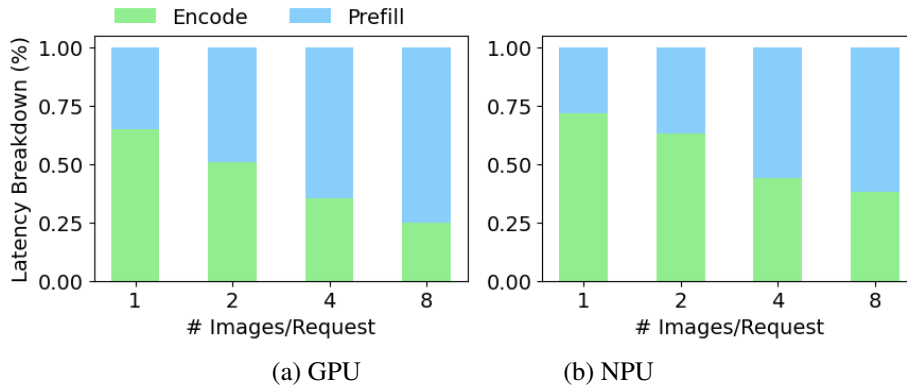


Figure 11. Breaking down the latency of encode and prefill for InternVL2-8B across different number of images per requests. We compare the difference between GPU (left) and NPU (right) where light green is encode and light blue is prefill.

### D.3. Heavier Encode in NPUs

We compare the encode-to-prefill stage latencies between NPUs and GPUs. Figure 11 show the results for the InternVL2-8B model, across various I/R values. As seen, we notice higher ( $\approx 10 - 20\%$ ) encode-to-prefill latency ratios for NPUs in comparison to GPUs, indicating the need for a different optimized configuration for NPU.

This trend was consistent across different large multimodal models (LMMs), indicating that NPUs tend to spend a greater proportion of time in the encoding phase compared to GPUs.